

## RESEARCH ARTICLE

10.1002/2017JB014593

## Key Points:

- An array analysis method is developed to locate microseism sources in the Atlantic Ocean from correlation functions
- Strong sources generate spurious arrivals that can be identified in the correlation functions

## Correspondence to:

L. Retailleau,  
retailleu@stanford.edu

## Citation:

Retailleau, L., Boué, P., Stehly, L., & Campillo, M. (2017). Locating microseism sources using spurious arrivals in intercontinental noise correlations. *Journal of Geophysical Research: Solid Earth*, 122, 8107–8120. <https://doi.org/10.1002/2017JB014593>

Received 21 JUN 2017

Accepted 9 SEP 2017

Accepted article online 14 SEP 2017

Published online 26 OCT 2017

## Locating Microseism Sources Using Spurious Arrivals in Intercontinental Noise Correlations

Lise Retailleau<sup>1,2</sup> , Pierre Boué<sup>1</sup> , Laurent Stehly<sup>1</sup>, and Michel Campillo<sup>1</sup>
<sup>1</sup>Institut des Sciences de la Terre, CNRS, Université Grenoble Alpes, Grenoble, France, <sup>2</sup>Now at Department of Geophysics, Stanford University, Stanford, CA, USA

**Abstract** The accuracy of Green's functions retrieved from seismic noise correlations in the microseism frequency band is limited by the uneven distribution of microseism sources at the surface of the Earth. As a result, correlation functions are often biased as compared to the expected Green's functions, and they can include spurious arrivals. These spurious arrivals are seismic arrivals that are visible on the correlation and do not belong to the theoretical impulse response. In this article, we propose to use Rayleigh wave spurious arrivals detected on correlation functions computed between European and United States seismic stations to locate microseism sources in the Atlantic Ocean. We perform a slant stack on a time distance gather of correlations obtained from an array of stations that comprises a regional deployment and a distant station. The arrival times and the apparent slowness of the spurious arrivals lead to the location of their source, which is obtained through a grid search procedure. We discuss improvements in the location through this methodology as compared to classical back projection of microseism energy. This method is interesting because it only requires an array and a distant station on each side of an ocean, conditions that can be met relatively easily.

## 1. Introduction

Seismic ambient noise in the microseism frequency band is the continuous oscillation of the Earth as a result of the interactions among the atmosphere, the oceans, and the solid Earth (Ebeling, 2012). When studying earthquake data, seismic ambient noise has been seen as a nuisance that blurs the signal of interest. However, it has been shown in recent decades that seismic ambient noise also carries information about the Earth interior. It has been demonstrated both theoretically and through laboratory experiments that the correlation functions of long time series of ambient noise recorded at two seismic stations converge toward the Green's function between these two stations (Derode et al., 2003; De Verdière, 2006; Wapenaar, 2004). Basically, this means that under certain conditions, the correlation function between two stations represents a way to study the wave propagation that would be observed if a source had been fired at one of the stations and recorded at the other (Weaver & Lobkis, 2004). When considering seismic data, these correlation signals thus constitute a valuable supplement to earthquake data, as they can provide the Green's function between any pair of receivers (Shapiro & Campillo, 2004) and can thus allow the analysis of areas that do not have earthquakes.

Indeed, seismic noise correlations have turned out to be an efficient tool for surface wave tomography (i.e., Lin et al., 2013; Sabra et al., 2005; Shapiro et al., 2005; Shen & Ritzwoller, 2016) and for monitoring temporal variations of the Earth crust associated with, for instance, earthquakes and volcanic eruptions (Brennguier, Shapiro, Campillo, Ferrazzini, et al., 2008a; Brennguier, Shapiro, Campillo, Hadzioannou, et al., 2008b; Sens-Schönfelder & Wegler, 2006).

However, the assumptions that ensure that correlation functions are similar to the Green's functions are restrictive, as they require the wavefield to be equipartitioned, which means that all of the modes are excited incoherently with the same level of energy (Sánchez-Sesma & Campillo, 2006). For a two-dimensional acoustic medium, which represents a good analog to single-mode Rayleigh wave propagation, this condition can be met if the sources are evenly distributed within the medium and/or the scattering of the waves on heterogeneities is strong enough to randomize the wavefield (Derode et al., 2003; Wapenaar et al., 2006; Weaver & Lobkis, 2001). In practice, microseism sources are restricted to the free surface of the Earth, which implies that the seismic noise is dominated by surface waves (Bernard, 1952; Ekström, 2001; Friedrich et al., 1998; Hasselmann, 1963). At periods > 1 s, the coupling of oceanic swells with the solid Earth is mostly responsible

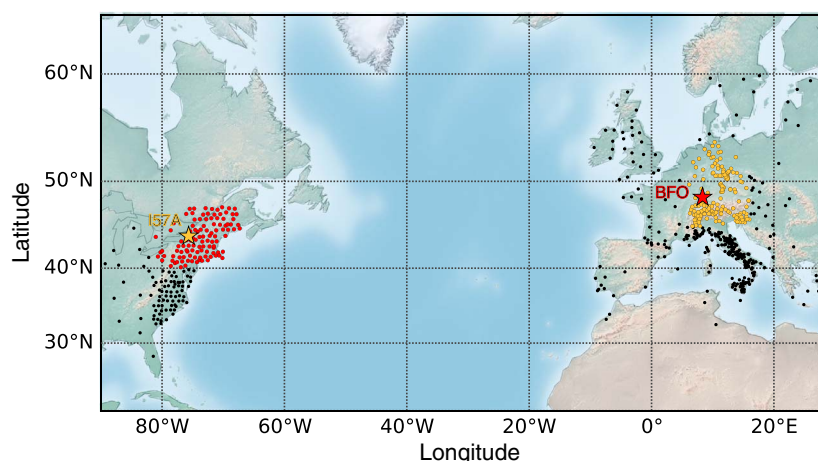


**Figure 1.** Map of the 900 broadband stations available on opposite sides of the Atlantic Ocean. The red and orange points represent the two subnetworks used for the analysis of the spurious arrivals (110 in the U.S. and 174 in Europe). The two stars represent the stations used as the references on the opposite sides of the Atlantic Ocean (BFO in Germany and I57A in the U.S.).

for the ambient seismic field excitation (Kedar et al., 2008; Longuet-Higgins, 1950; Nishida et al., 2008, 2000; Stutzmann et al., 2000; Webb, 1998). The strongest signal is called the microseismic noise, the spectrum of which is dominated by two peaks: the primary microseism between 10 s and 20 s, and the secondary microseism between 3 s and 10 s. Both of these microseisms are generated by the interactions between oceanic waves and the solid Earth that generate pressure at the ocean bottom, which is then converted into elastic waves (e.g., Ardhuin et al., 2011; Bromirski et al., 2005, 1999; Farra et al., 2016; Kimman et al., 2012). Moreover, bathymetry also has a key role, as it controls the coupling between the ocean and the solid Earth (Gualtieri et al., 2014; Kedar et al., 2008; Longuet-Higgins, 1950). Finally, the generation of seismic noise is influenced by the occurrence of strong storms, and thus it shows temporal variations. Consequently, microseism sources are never perfectly homogeneously distributed within space, time, and frequency, which usually results in an incomplete or biased Green's function recovered from the correlation functions.

In this article, we analyze the Rayleigh wave that is generated by microseism sources in the North Atlantic Ocean using seismic noise correlations. Though we do not cover its analysis, the Love wave has been shown to be strongly excited by microseism sources (Matsuzawa et al., 2012; Nishida et al., 2008). Other analyses have discussed the theoretical generation mechanism of Love wave (Fukao et al., 2010; Saito, 2010). Juretzek and Hadziioannou (2016) used Love-to-Rayleigh ratios in order to locate ocean microseism sources using three-component beamforming.

Our data set consists of 1 year (2014) of continuous seismic data that was recorded by the vertical component of roughly 900 broadband stations in Europe and in the U.S. (Figure 1). The data were downloaded from the Incorporated Research Institutions for Seismology (IRIS, <http://www.iris.edu/mda>) and European Integrated Data Archive (EIDA, <http://www.orfeus-eu.org/eida/eida.html>) Data Services. The detailed network list and the corresponding data centers used are described in Appendix A.

In the first section, a classical backprojection approach is applied to measure the ambient noise directionality due to the dominant North Atlantic Ocean microseism sources, as seen by a regional tomography setting, which is a main use of the correlation functions, using the European subnetwork (Figure 2b) in the period band of 15 s to 25 s. Here Stehly et al. (2006) and Ermert et al. (2016) are followed, who based their detections on measurement of the amplitude ratio between causal and anticausal parts of the correlation functions. The resolution and limitations of this method are discussed in comparison to the present approach. In the second section, while remaining in the 15 s to 25 s period band, these Northern Atlantic sources are further analyzed by choosing a different station configuration that involves cross-Atlantic interstation paths. An array that contains a regional subnetwork (e.g., for the U.S. side: Figure 1, red points) and a distant, cross-Atlantic, station (e.g., station BFO in Europe: Figure 1, red star). This configuration was chosen so that the sources can be considered between the subnetwork and the distant station. This purposely leads to biased reconstructed Green's functions that can be used to precisely locate the dominant sources. Indeed, such sources generate

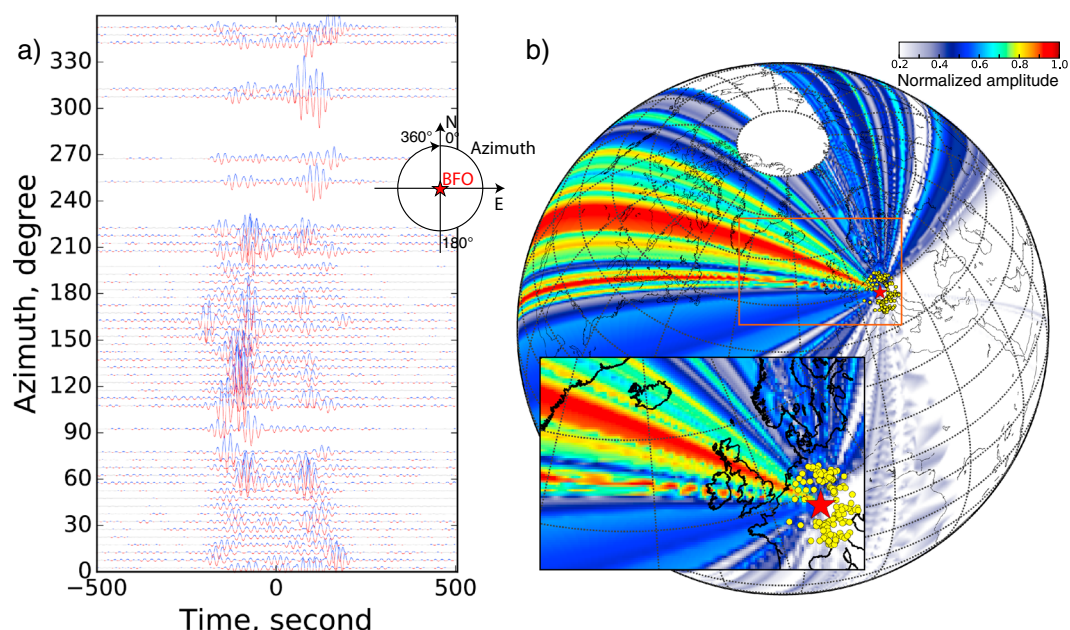


**Figure 2.** (a) Correlations computed between BFO and the 145 European stations at distances from 200 km to 500 km, filtered in the period band of 15 s to 25 s, and represented as a function of the azimuth of each station pair. For visualization, the correlations are stacked on 5° of azimuth bins. (b) Backprojection result computed from the amplitudes of the correlations functions. Station BFO is shown as the red star, and the other stations used are shown as yellow dots.

precursory arrivals on the correlation functions, which are also designated as spurious phases (Kimman & Trampert, 2010; Shapiro et al., 2006; Tian & Ritzwoller, 2015; Zeng & Ni, 2010). Slant stack processing is performed on these spurious phases that are detected on the correlation functions computed by station pairs formed between the distant station and the different subnetwork stations. A grid search procedure then leads to the locating of the sources.

For the sake of illustration clarity, we first analyze the correlation functions filtered in the period band of 15 s to 25 s, which showed the best signal-to-noise ratio. In the last section, after discussing the results for this period band, we also discuss lower (10–20 s) and higher (30–50 s) period bands, as well as the 26 s microseism source (e.g., Shapiro et al., 2006).

## 2. Classical Approach: Wavefield Directionality Using Correlation Symmetries

In this section, we measure the ambient seismic wavefield directionality to evaluate the distribution of the Rayleigh wave microseism sources. The approach here is based on the amplitude ratio of the intracontinental correlation functions computed on a European broadband subnetwork, following the methodology introduced by Stehly et al. (2006) and applied by Yang and Ritzwoller (2008) and Ermert et al. (2016). This represents an alternative method to direct wavefield backprojection (e.g., Gerstoft et al., 2006; Kedar et al., 2008; Nishida & Takagi, 2016). The spatial distribution of the stations is here similar to a regional tomography configuration.

### 2.1. Station Settings and Methodology

A single station (BFO) located in the Black Forest, Germany, is used as the reference station (Figures 1 and 2b, red star). Correlation functions are computed between this reference station and 145 other European broadband receivers (Figure 2b, yellow points). The interstation distances range from 200 km to 500 km.

As for all the correlation functions used in this study, the main processing steps are as follows: (1) correction of the instrumental response of all of the daily records; (2) splitting of the daily records into 4 h segments and discarding those with strong transient energy (i.e., with earthquakes); (3) broadband frequency domain normalization (i.e., whitening) and soft clipping in the time domain to remove any remaining bursts of energy. We do not apply one-bit nor temporal normalization to avoid changing the physical source distribution; (4) correlation over all of the 4 h time windows and stack over the year; and (5) filtering in the period of interest, that is, the 15 s to 25 s period.

Figure 2a shows the resulting correlation functions that were computed between BFO and 145 European receivers, sorted by azimuth. The anticausal part corresponds to the waves that travel from BFO to the other stations, and the causal part is the other way around. We observe that the approximate Rayleigh waves reconstructed are not symmetric: the waves do not have the same amplitude for the causal and anticausal parts. The amplitudes are larger for the anticausal part for azimuths ranging from  $50^\circ$  to  $230^\circ$  and in the causal part outside of this range. This suggests that the dominant noise sources are located northwest of BFO.

Following Stehly et al. (2006), we use this lack of symmetry in the amplitude of the reconstructed Rayleigh wave to evaluate the directionality of the original ambient seismic wavefield. The azimuthal resolution is defined by the azimuthal distribution of all of the station pairs (i.e., BFO versus the others). The measurements are corrected from the geometrical attenuation of the Rayleigh waves with distance, by multiplying the amplitude by the square root of the interstation distance (200–500 km). For each correlation, the normalized amplitude of the seismic noise that propagates along two azimuths is measured. Combining the measurements from each station pair, the distribution of the normalized amplitude with respect to azimuth is obtained.

## 2.2. Backprojection of the Amplitude Information to Locate Microseism Sources

To map the distribution of the microseism sources that contribute to the Rayleigh wave reconstruction, a simple backprojection procedure is used that is based on the great circle path defined by each station pair. The Rayleigh wave amplitudes measured for the causal and anticausal correlation parts are attributed to their corresponding half great circle. This is of course an approximation, on the basis that (1) we do not take into account the finite frequency effect, which means that we use ray theory in a homogeneous medium; and (2) the path followed by the Rayleigh waves is not necessarily a great circle, because of crustal and upper mantle heterogeneities. Finally, the amplitudes along each great circle path are mapped on a  $0.5^\circ \times 0.5^\circ$  regular grid on the Earth surface. If several paths cross the same cell, the amplitudes are averaged.

The resulting map of the distribution of noise sources is shown in Figure 2b. As we used a single network located in Europe, there is decent azimuthal resolution but no possibility to evaluate the distance of the source with respect to the network. We see that the Rayleigh wave energy comes mostly from the northwest. The Rayleigh waves coming from other azimuths have much lower energy. This is an expected result, as it is well known that the microseism ambient field under 1 Hz recorded in Europe is dominated by sources located in the North Atlantic Ocean (Chevrot et al., 2007; Friedrich et al., 1998; Hillers et al., 2012; Kedar et al., 2008). More precisely, we measure two azimuthal ranges associated with two dominant sources: a broad one around  $340^\circ$  east and a narrow one at about  $300^\circ$  east.

Backprojection of the amplitude ratio of the Rayleigh waves measured for correlation functions computed within an intracontinental network provides a simple but efficient way to map the azimuthal distribution of microseism sources with reasonable resolution. However, this simple method does not provide any information about the distances of the sources if a single array is used. To more precisely map the location of the source within the Ocean, at least two networks should be used simultaneously, where the source location is the area where the two high amplitude backprojections cross each other. The resolution would then be defined by the location of both of the arrays relative to the source, similar to a basic triangulation problem. In the following section, a new methodology is introduced to locate oceanic microseism sources by simply adding a trans-Atlantic seismic station to a single regional deployment, similar to that used in Figure 2.

## 3. Locating the Noise Sources Using Spurious Arrivals in the Correlation Functions

The proposed approach is based on the analysis of the Rayleigh wave spurious arrivals that appear on the trans-Atlantic correlation functions. Zheng et al. (2011) observed a spurious arrival and associated it to the localized persistent Kyushu microseism highlighted by Zeng and Ni (2010) and Zeng and Ni (2011). The presence of these spurious arrivals results from the nonhomogeneous distribution of noise sources and the presence of dominant and localized microseism sources, which implies that noise correlations do not converge properly toward the Green's function.

### 3.1. Observation of Spurious Phases

It is well known that in the absence of a strong scattering regime, the source distribution has a very important impact on the noise correlation function obtained between two receivers. This impact is also relative to the frequency band considered. For a simple two-dimensional homogeneous medium, Figure 3a shows the arrival time of a source for a correlation computed between the two receivers A and B, as a function of the source location in two dimensions and its representation on the Earth. The sources are here regularly distributed



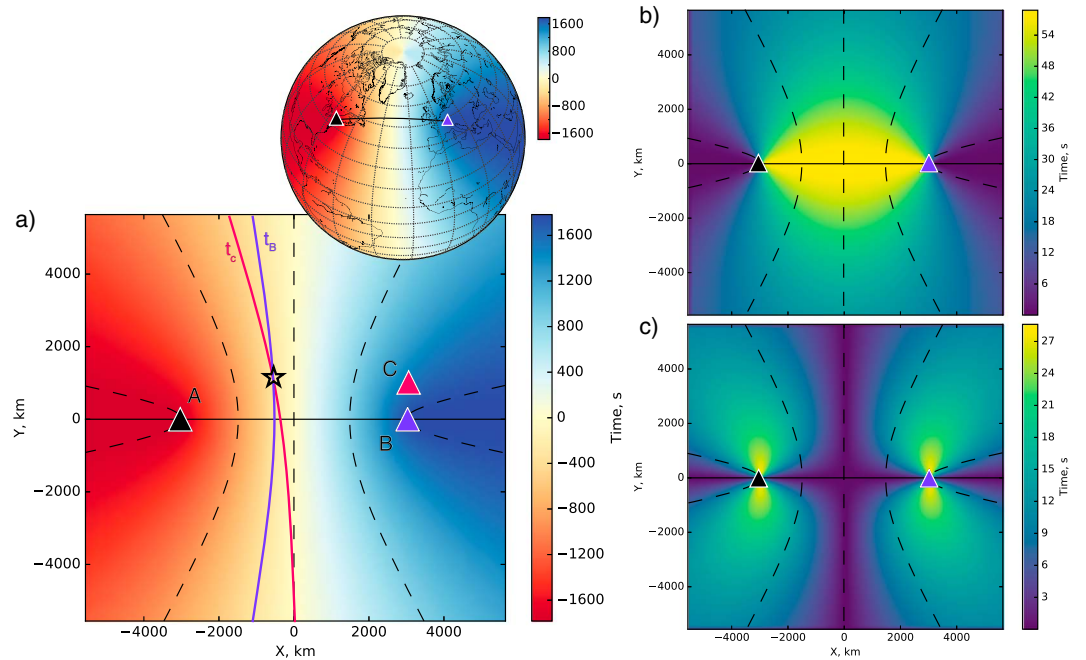


**Figure 3.** (a) Color map representation of the differential arrival times between the arrival time from the source to station A and the source to station B as a function of the source location, and its representation on the Earth. This is equivalent to the arrival time of the source on a correlation function computed between the two receivers, A and B. We assume constant velocity  $V = 3.4 \text{ km s}^{-1}$ . The dashed hyperbolae show several iso-arrival times. The two continuous blue and pink lines represent the two iso-arrival times (hyperbolae) for the correlations A-B and A-C (C being another receiver), respectively, associated with a source at the black star. Gradient of arrival time from Figure 3a for increments of 100 km: (b) on the x axis and (c) on the y axis.

across the medium. This arrival time  $t_i$  is simply the difference in the traveltime from each source  $s$  to the two stations A and B:

$$t_i(r_s) = V \cdot d(r_s, r_{\text{ref}}) - V \cdot d(r_s, r_i), \quad (1)$$

The velocity is fixed here to  $V = 3.4 \text{ km s}^{-1}$ , and  $d(r_s, r_{\text{ref}})$  is the distance in kilometers between the source position  $r_s$  and the distant station position  $r_{\text{ref}} = r_A$  (Figure 3a, A). We name the reference station as the isolated station far from the regional network, A in the example in Figure 3a. The parameter  $d(r_s, r_i)$  is the distance between the source and the position  $r_i = r_B$  of a station belonging to the regional network (Figure 3a, B). As defined by convention, negative apparent traveltimes (i.e., anticausal arrivals) indicate a source closer to the reference station.

Sources spread and distributed in a two-dimensional medium that release similar energy would interfere destructively, except for those located in the so-called end-fire lobes (also known as the Fresnel zones or the stationary phase regions; Roux et al., 2005; Snieder, 2004). Sources that are inside these regions contribute constructively to the direct waves that travel between A and B: in our case the ballistic Rayleigh wave. On the other hand, a dominant and small enough source outside the end-fire lobes would generate a signal precursory to the Rayleigh waves arrival time for the correlation (Kimman & Trampert, 2010; Shapiro et al., 2006; Tian & Ritzwoller, 2015; Zeng & Ni, 2010). These kinds of precursory arrivals, which are often designated as spurious arrivals, have been considered a nuisance because they can dominate the expected Green's function and bias the velocity measurements in imaging applications.

We propose to make use of these spurious arrivals to locate microseism sources in the Atlantic Ocean. To that end, we use the correlation functions computed between the U.S. and Europe (Figure 1), as described in the previous section. Figure 4a illustrates the correlations computed between a station in Germany (BFO; Figure 1, red star) and a network of 110 broadband receivers located in the U.S. (Figure 1, red points). The correlations are sorted as a function of the interstation distances and are filtered between periods of 15 s and 25 s. The anticausal part shows waves traveling from the reference station in Europe to the U.S. The amplitude of the direct Rayleigh wave (Figure 4a, dark blue, red arrows) is larger in the causal part, which indicates that there

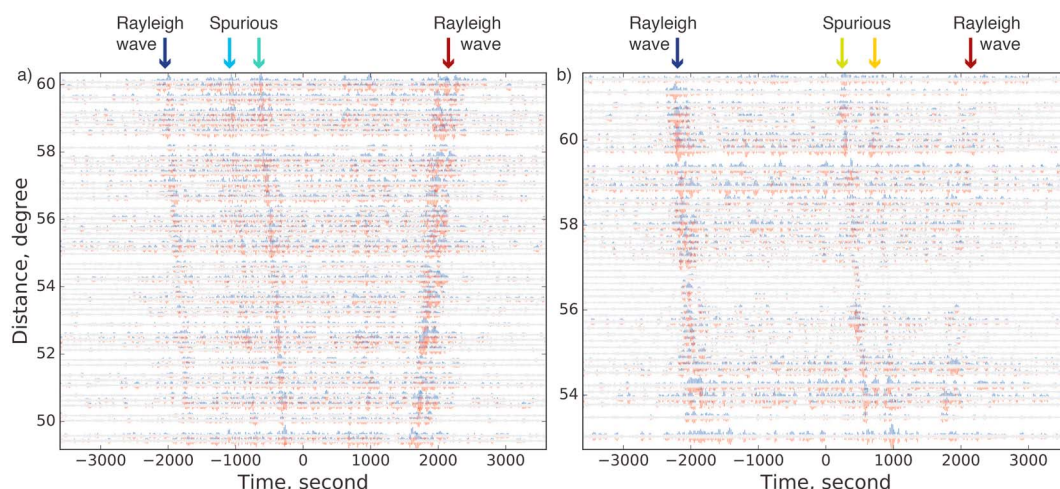


**Figure 4.** Correlation functions computed between a subnetwork and a distant, trans-Atlantic station filtered for the period band 15 s to 25 s. For the sake of clarity, the signals are averaged in 0.15° distance bins. (a) Correlations between station BFO in Europe and the subnetwork in the U.S. (b) Correlations between I57A in the U.S. and the subnetwork in Europe.

is more energy coming from the west/south of the U.S. stations than from the south/east of BFO. In addition to the Rayleigh wave propagating between BFO and the U.S. subnetwork, spurious arrivals appear for the anticausal part of the correlation functions (Figure 4a, light blue, green arrows). This is confirmed by a symmetrical configuration using a reference station on the U.S. side (I57A; Figure 1, orange star) and a network of broadband receivers in Europe (Figure 1, orange points). Here the positive time corresponds to waves traveling from Europe to the U.S. As before, the spurious phases clearly indicate a source located closer to Europe than to the U.S. (Figure 4b). In the next paragraph, we make use of the spurious arrival time to evaluate the dominant source locations.

### 3.2. Locating the Dominant Microseism Sources Using a Grid Search

In a two-dimensional homogeneous medium, the sources that can contribute to correlations computed between a pair of receivers  $A$ - $B$ , at a given time  $t_s$ , are located along a hyperbola (Figure 3, dashed lines). Consequently, a dominant source (e.g., at the location of the black star in Figure 3) would generate a spurious arrival on the correlation between station  $A$  and  $B$  that can only be located along a hyperbola (Figure 3, blue line). Similarly, the spurious phase generated by the same source for the correlation between receiver  $A$  and a new station  $C$  indicates that the source is located on another hyperbola (Figure 3, pink line). By measuring the arrival time of a spurious signal due to the same source for correlations computed between two station pairs  $A$ - $B$  and  $A$ - $C$ , two hyperbolae are obtained that intersect at the location of the source (Figure 3, blue, pink lines). This simple example illustrates that the measuring of the arrival time of a spurious phase on two correlation functions (i.e., different station pairs) leads to the location of the source of this arrival by simple geometrical construction.

Figures 3b and 3c represent the gradient of time arrivals of the different potential spurious sources over a 100 km  $\times$  100 km grid in the  $x$  and  $y$  axes using two stations ( $A$  and  $B$ ). Therefore, Figure 3b represents the variation of time arrivals on the correlation functions for two sources separated by 100 km along the  $x$  axis. Both Figures 3b and 3c indicate a small time variation in the end-fire lobes indicating the stationary phase zone. The figures show that the time variations diminish with distance to the great circle between the stations, thus diminishing the resolution. Therefore, the sources away from the great circle should appear smeared compared to the sources close to the great circle. They also indicate the limit of source period that can be resolved on a 100 km  $\times$  100 km, with the maximum being a period of 58 s between the two stations. These figures correspond to a couple of stations; thus, we expect that the supplementary stations should increase the domain of possible source characterization.

To locate microseism sources in the Atlantic Ocean, we use correlation functions computed between a reference receiver located in Europe and a subnetwork of stations in the U.S. (or the opposite, similar to those shown in Figure 4). First, the Rayleigh phase velocity is measured (equation (1),  $V$ ) by computing a vespagram from the noise correlation functions at the expected time of arrival of the Rayleigh wave that propagates

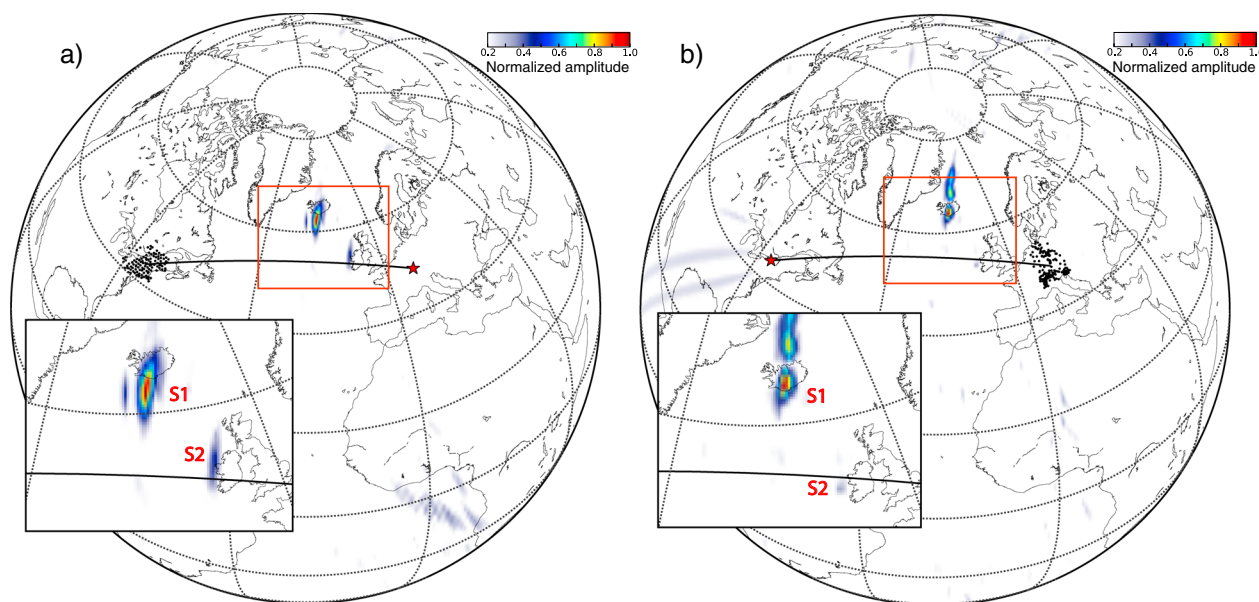


**Figure 5.** Results of the grid search  $S(r_s, t = 0)$  for the Earth surface using the correlations filtered in the period band of 15 s to 25 s computed (a) between reference station BFO in Europe and a network in the U.S. and (b) between reference station I57A in the U.S. and a network in Europe.

from BFO to the U.S. subnetwork for the anticausal part and the opposite for the causal part. The velocities obtained for the causal and anticausal parts are then averaged. In the period band of 15 s to 25 s, the velocity obtained is 3.6 km/s, which is consistent with the fundamental Rayleigh wave velocity in the isotropic PREM model (Dziewonski & Anderson, 1981).

Then, we define a regular  $1 \times 1^\circ$  grid at the surface of the Earth as potential source locations. For each station pair  $i$  considered, using equation (1) we compute the arrival time  $t_i(r_s)$  that would be measured on the corresponding correlation function if a source was fired at the location  $r_s$  defined by each position on the grid. The data (i.e., the correlation gathers) are then time shifted according to the expected  $t_i(r_s)$  and then stacked. This processing is equivalent to a slant stack applied to the correlation data sets defined as a function of the source location, and it can be summarized as follows:

$$S(r_s, t) = \sum_{i \in \text{station pairs}} C_i(t - t_i(r_s)) \quad (2)$$

where  $S(r_s, t)$  is the stacked correlation function that has been corrected for a singular source located at  $r_s$ , and  $C_i$  is a correlation function for a particular trans-Atlantic station pair  $i$ . We do not apply any geometrical spreading correction in this analysis.

We finally calculate the envelope of  $S(r_s, t)$  using the absolute value of the Hilbert transform. At  $t = 0$ ,  $S(r_s, t)$  simply characterizes the amplitude of the spurious phase that would be generated if a dominant microseism source was located at the location  $r_s$ . As a probability of the presence of a source at a given location, mapping  $S(r_s, t = 0)$  is equivalent to mapping the dominant sources. The assumption that the velocity  $V$  is constant and equal to that reconstructed between the reference station and the array implies that the quality of the location decreases when the source is farther from the great circle connecting the stations. Figure 5 illustrates some examples of this grid search that are obtained from the trans-Atlantic correlations filtered in the period band of 15 s to 25 s. In Figure 5a, we use the signals shown in Figure 4a, where the network is in the U.S. and the reference station is in Europe (BFO). In Figure 5b, we use the signals shown in Figure 4b, where the network is in Europe and the reference station is in the U.S. (I57A).

#### 4. Discussion

Figure 5 indicates a main source of energy S1 south of Iceland and a potential secondary, but less energetic, source S2 on the west coast of Ireland (Figure 5b, relatively low amplitude). Also, S1 spreads northward in Figure 5b. It has to be noted that we do not apply any muting of the grid search over continental or island areas, even if we do not expect any microseism sources inland. Figures 3b and 3c show that the location resolution of

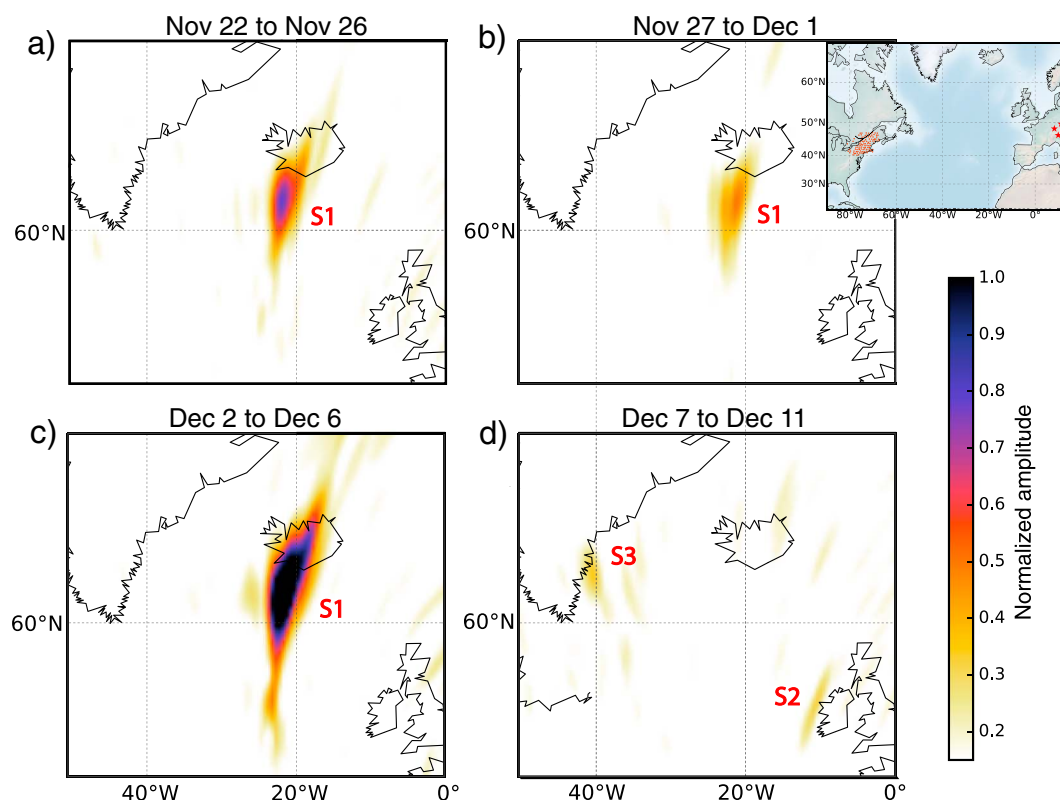


**Figure 6.** Source location using the spurious arrivals for four consecutive 5 day stack correlations. The map represents the stations used. The amplitudes are normalized by the maximum amplitude over the year. The U.S. network is represented by the red points, and the three reference stations are represented with stars.

the proposed method diminishes with distance to the great circle between the stations. This can explain the spreading of the source S1, which is partly inland. Our assumption of a homogeneous medium (i.e., constant velocity) could also generate bias for the location which would increase away from the great circle between the stations.

The observations of S1 and S2 are consistent with results obtained by analyzing the amplitude ratios of the noise correlations computed in Europe presented in section 3 (Figure 2b). The main difference between the two results is that our approach constrains both the azimuth and the source distance, whereas only the azimuth was measured using the amplitude ratio method (Figure 2b). To constrain the distance of the source with the amplitude ratio method, it would be necessary to perform the same method on a second array at a useful location and cross the results. The result would then be a superposition of the two backprojections. In the spurious analysis method we have only one supplementary station, a condition that is more easily met than finding an array.

To go a step further in the analysis of the microseism sources, it is also possible to carry out such measurements for a shorter time window. Instead of using correlation functions that have been stacked over a full year, we here propose to use the 5 day averages. Figure 6 shows the same sources as Figure 5 but for four different time windows. The short time window average leads to a lower signal-to-noise ratio that we can improve by spacial averaging. Each map of Figure 6 is actually an average over three  $S(r_s, t=0)$  results, using different reference stations (Figure 6, inset). The four panels of Figure 6 correspond to time windows centered on 24 and 29 November and 4 and 9 December (Julian days 328, 333, 338, and 343, respectively).

The main source of noise S1 located south of Iceland is visible for three dates (24 and 29 November and 4 December; Figures 6a–6c). Its position remains the same, which suggests that the observation is associated either with a scattering effect on the Rayleigh waves at the Iceland coast or the local bathymetry, or an interaction between the oceanic waves and the coast or bathymetry, to generate Rayleigh waves.

No other sources appeared during this period. As shown in Figure 6d, no noise source was detected south of Iceland on 9 December. Instead, the second source S2 is visible for the west coast of Ireland. A smaller



source S3 also appears along the east coast of Greenland. These two sources appear to be located along the coastline and might be generated in the same way as source S1. The different times of the appearances of source S1 versus sources S2 and S3 might suggest two different origins. It might also suggest that the waves that generate source S1 are actually reflected and lead to sources S2 and S3. As an example, oceanic waves at 20 s period propagate with a velocity of about  $31 \text{ m s}^{-1}$ , which leads to a propagation time of about 17 h from the south of Iceland to the west of Ireland (Sorensen, 2005), which might be short to observe sources S1 and S2 at different times.

These results show that this method makes it possible to study the temporal evolution of the noise sources with a resolution down to 5 days in the 15 s to 25 s period band. Figure 6 shows that the proposed approach allows spatiotemporal monitoring of microseism sources with good resolution in this period band (i.e., 15–25 s).

Up to this point, all of the results shown here are based on correlations filtered in the period band of 15 s to 25 s. Figure 7 presents the distribution of the noise sources obtained for three other period bands: 10 s to 20 s (a, b), 30 s to 50 s (c, d), and 25 s to 27 s (e, f). Figures 7a–7d were computed using the same station configuration as that used to compute Figure 5a. In each case, the velocity  $V$  is extracted from the vespagram computed with the correlations filtered in the chosen frequency band.

The correlation functions filtered from 10 s to 20 s, which correspond to the first microseism peak, are represented in Figure 7a and show blurry spurious arrivals (red arrow). Figure 7b shows the grid search result for the corresponding period band. The two sources S1 and S2 are still visible but with lower signal-to-noise ratios compared to Figure 5. It is particularly important to remember here that the correlations used correspond to trans-Atlantic distances, and thus even the first microseism peak can be considered a relatively high frequency for surface wave propagation. This might explain these signal-to-noise ratio differences between Figures 5a and 7b: the spurious arrival is much more coherent at long periods, even though we expect stronger excitation in the first and second microseism peaks.

For the longer period using the correlation functions filtered between 30 s and 50 s, Figure 7c clearly shows a single spurious arrival (red arrow). The grid search presented in Figure 7d indicates that it corresponds to source S1 located near Iceland, as for the 15 s to 25 s period band (Figure 5). At this long period band, the ballistic Rayleigh wave is very coherent, which also leads to a reconstruction of the end-fire lobes linked to an apparent source distribution that reconstructs the Green's function. While the location of source S1 is consistent with the other frequency bands, the source location in Figure 7d is largely spread over Iceland, although as discussed before, we do not expect sources inland. The energy spot widens with the increasing period, which might explain why the spot is most spread inland in the period band of 30 s to 50 s. Another cause for this spread of the locations is the approximation of a homogeneous propagation medium; that is, the use of a constant velocity in the location process. To decrease the bias associated with our assumption, our method can be improved by iteratively performing a grid search over the source distribution and the Rayleigh wave velocity: after initial source location, a set of velocities can be tested to reach a better signal-to-noise ratio in the slant stack. The velocity from the source to the two stations of the pair might also be different. This simple step would then lead to a new location that would be more accurate. It would also result in effective imaging of the travel paths covered.

An important observation is that source S1 appears in the period band of the primary microseism and the two longer period bands (Figures 5, 7a, and 7b). As Rhie and Romanowicz (2006) suggested, the long periods might be generated by the nonlinear interactions between the shorter period waves and the coast, which generates gravity waves that interact with the seafloor locally and generate long period waves. Ardhuin et al. (2015) argued that long-period sources originate from shelf breaks and that they are generated by ocean waves of the same period. A thick sedimentary layer along the coast of Greenland could influence the microseism excitation and be the scatterer observed. The analysis of the horizontal components and thus of the Love wave extracted from correlations could also give information about the excitation mechanism of microseisms. Fukao et al. (2010) and Saito (2010) suggested that a linear topographic coupling between the ocean and seismic waves could explain the generation of the Love wave.

Finally, Figures 7e and 7f show the distribution of the noise sources obtained in the 25 s to 27 s period band. We specifically selected this period band based on previous observations and studies of a 26 s period source located in the Guinea Gulf (e.g., Bernard & Martel, 1990; Holcomb, 1980; Oliver, 1962; Shapiro et al., 2006;

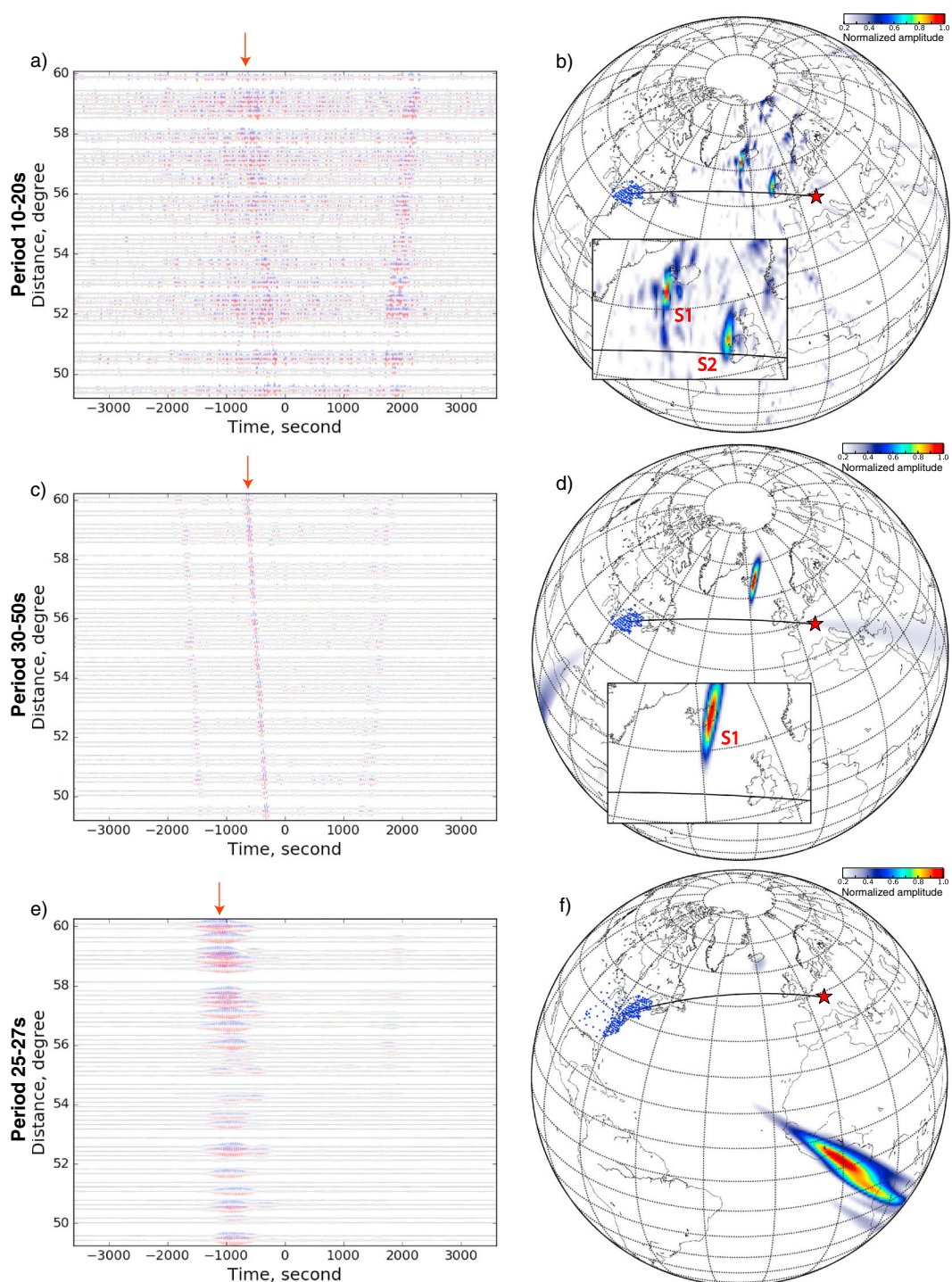


**Figure 7.** Correlations filtered for the period bands of (a) 10 s to 20 s, (c) 30 s to 50 s, and (e) 25 s to 27 s. Results of the grid search  $S(r_s, t = 0)$  computed at the Earth surface for the period bands of (b) 10 s to 20 s, (d) 30 s to 50 s, and (f) 25 s to 27 s.

Zeng & Ni, 2010, 2014). Here we use the correlation functions between all of the available stations in the eastern U.S. and the single station BFO in Germany (Figure 7f, blue points, red star, respectively). The long duration of this spurious arrival is linked to the narrow period band chosen. We clearly observe a spurious arrival associated with this source (Figure 7e, red arrow). Even if the expected source location is actually far from the great circle between BFO and the subnetwork in the U.S., we are able to retrieve it in the Gulf of Guinea with reasonable resolution, in agreement with the literature on this source.

## 5. Conclusions

Correlation of ambient seismic noise between two receivers is commonly used as an empirical Green's function between the two receivers, either to image or to monitor the subsurface. Such applications are usually performed in the microseism frequency band or at even lower frequencies (i.e., hum). It is also well known that the convergence of the correlation functions toward the expected Green's function is very sensitive to the distribution of the microseism sources. If a source dominates in particular, it might bias the correlation function by generating a spurious arrival before the arrival that corresponds to the Green's function. Both the location of the receivers (i.e., relative to the sources) and the complexity/heterogeneity of the medium (i.e., relative to the frequency band) can also have important roles. In this article, we intentionally selected a case where the correlations did not converge efficiently, meaning that spurious Rayleigh wave arrivals can be observed due to the strong quasi-punctual sources. These correlation functions are computed using a selection of stations that involves trans-Atlantic interstation paths (i.e., an array and a distant station).

Based on such a correlation data set, we proposed a simple methodology to locate the dominant microseism sources in the Atlantic Ocean that are responsible for the spurious arrivals. We presented results for the year 2014 in four different period bands: 15 s to 25 s, 10 s to 20 s, 25 s to 27 s, and 30 s to 50 s. Compared to classical beamforming/backprojection approaches, our grid search analysis allows the location of the source based on a velocity assumption (constant in this case). These measurements in the 15 s to 25 s period band are still consistent with the azimuth found using classical backprojection: both indicate a dominant source south of Iceland and a weaker one northwest of Ireland. It has to be noted that this method only detects dominant sources that are responsible for spurious arrivals and would not allow the characterization of an extended smooth source distribution. Moreover, we also showed that temporal evolution of the source location and amplitude can be measured with resolution down to a few days and with a very good signal-to-noise ratio. Finally, different period bands from the first microseism up to 50 s were explored. The results from the 26 s microseism match previous studies, even if the source region (Gulf of Guinea) is far from the great circle between the station selection in the present study. In this article, we used a constant velocity measured from

**Table A1**  
*The Seismological Networks Used in Europe*

Network	N stations	Data center
BW	1	LMU, Germany; Department of Earth and Environmental Sciences, Geophysical Observatory, University of Munchen (2001)
CH	33	ETH, Switzerland (Swiss Seismological Service (SED) at ETH Zurich, 1983)
CR	1	Croatian Seismograph Network (University of Zagreb, Croatia)
CZ	13	Czech Regional Seismic Network (Institute of Geophysics, Academy of Sciences of the Czech Republic, 1973)
FR	33	RESIF, France (RESIF, 1981)
G	3	Geoscope, France (Institut de Physique du Globe de Paris (IPGP), 1982)
GE	16	GFZ, Germany (GEOFON Data Centre, 1993)
GR	43	BGR, Germany
IV	139	INGV, Italy
MN	17	INGV, Italy
NL	1	ODC, Netherlands
OE	11	Austrian Seismic Network (ZAMG—Central Institute for Meteorology and Geodynamics, Austria)
SI	6	INGV, Italy
SL	22	Seismic Network of the Republic of Slovenia (Slovenian Environment Agency, 2001)
SX	11	SXNET Saxon Seismic Network (University of Leipzig, Germany)
TH	16	Thüringer Seismisches Netz (Institut fuer Geowissenschaften, Friedrich-Schiller-Universitaet Jena, Germany)

Note. N is the number of stations.

**Table A2**  
The Seismological Networks Used in the U.S.

Network	N stations	Data center
IU	6	Global Seismograph Network (GSN-IRIS/USGS), United States (Albuquerque Seismological Laboratory (ASL)/USGS, 1988)
LD	1	Lamont-Doherty cooperative Seismographic network (Columbia University, United States)
TA	177	USArray Transportable Array, United States (IRIS Transportable Array, 2003)
US	23	United States National Seismic Network, United States (Albuquerque Seismological Laboratory (ASL)/USGS, 1990)

Note. N is the number of stations.

a vesogram analysis. To overcome this downside, the location can be coupled with velocity analysis, which leads to simple imaging of the different travelpaths (as discussed in section 4).

Adding a single trans-Atlantic station to a regional deployment allows precise location of the origin of the dominant microseism source. Our illustration for the North Atlantic Ocean can be easily generalized to different source regions using coastal seismic stations and several regional arrays.

## Appendix A: Details of the Data Sets Used

The data sets used in this study were downloaded using the *obsPy* toolbox and more particularly the FDSN Web service client *obsPy.clients.fdsn* (Krischer et al., 2015). The two Tables A1 and A2 show the different networks and data centers used to obtain the data in Europe and the U.S.

### Acknowledgments

The facilities of IRIS Data Services, and specifically the IRIS Data Management Center, were used to access the waveforms, related metadata, and/or derived products used in this study (<http://www.iris.edu/mda>). The IRIS Data Services are funded through the Seismological Facilities for the Advancement of Geoscience and EarthScope (SAGE) Proposal of the National Science Foundation under Cooperative Agreement EAR-1261681. The European records used to compute the correlation functions were downloaded from the EIDA and Orfeus webservices (<http://www.orfeus-eu.org/eida/eida.html>). Computations were performed using Python. The “basemap” module was used to plot the maps. The “obsPy” module was used for downloading the data (Krischer et al., 2015). Most of the computations presented here were performed using the CIMENT infrastructure (<https://ciment.ujf-grenoble.fr>), which is supported by the Rhône-Alpes region (grant CPER07\_13 CIRA: <http://www.ci-ra.org>). This work was supported by a grant from Labex OSUG@2020 (Investissements d’avenir-ANR10LABX56). The authors acknowledge the support of the Simone and Cino del Duca Foundation, Institut de France. The authors thank Andreas Fichtner and an anonymous reviewer for their constructive remarks.

### References

- Albuquerque Seismological Laboratory (ASL)/USGS (1988). *Global seismograph network (GSN-IRIS/USGS)*, Albuquerque, United States: International Federation Of Digital Seismograph Networks. <https://doi.org/10.7914/SN/IU>, other/Seismic Network.
- Albuquerque Seismological Laboratory (ASL)/USGS (1990). *United States National Seismic Network*, International Federation Of Digital Seismograph Networks. <https://doi.org/10.7914/SN/US>, other/Seismic Network.
- Ardhuin, F., Gualtieri, L., & Stutzmann, E. (2015). How ocean waves rock the Earth: Two mechanisms explain microseisms with periods 3 to 300 s. *Geophysical Research Letters*, 42, 765–772. <https://doi.org/10.1002/2014GL062782>
- Ardhuin, F., Stutzmann, E., Schimmel, M., & Mangeney, A. (2011). Ocean wave sources of seismic noise. *Journal of Geophysical Research*, 116, C09004. <https://doi.org/10.1029/2011JC006952>
- Bernard, P. (1952). Microséismes et prévision de la houle. *Pontificiae Academiae Scientiarum Scripta Varia*, 12, 131–146.
- Bernard, P., & Martel, L. (1990). A possible origin of 26 s microseisms. *Physics of the Earth and Planetary Interiors*, 63(3–4), 229–231.
- Brenguier, F., Shapiro, N. M., Campillo, M., Ferrazzini, V., Duputel, Z., Coutant, O., & Nercissian, A. (2008a). Towards forecasting volcanic eruptions using seismic noise. *Nature Geoscience*, 1(2), 126–130. <https://doi.org/10.1038/ngeo104>
- Brenguier, F., Shapiro, N. M., Campillo, M., Hadzioannou, C., Nadeau, R. M., & Larose, E. (2008b). Postseismic relaxation along the San Andreas fault at Parkfield from continuous seismological observations. *Science (New York, N.Y.)*, 321(5895), 1478–81. <https://doi.org/10.1126/science.1160943>
- Bromirski, P. D., Flick, R. E., & Graham, N. (1999). Ocean wave height determined from inland seismometer data: Implications for investigating wave climate. *Journal of Geophysical Research*, 104(C9), 20–753.
- Bromirski, P. D., Duennebie, F. K., & Stephen, R. A. (2005). Mid-ocean microseisms. *Geochemistry, Geophysics, Geosystems*, 6, Q04009. <https://doi.org/10.1029/2004GC000768>
- Chevrot, S., Sylvander, M., Benhamed, S., Ponsolles, C., Lefèvre, J., & Paradis, D. (2007). Source locations of secondary microseisms in Western Europe: Evidence for both coastal and pelagic sources. *Journal of Geophysical Research*, 112, 2156–2022. <https://doi.org/10.1029/2007JB005059>
- Department of Earth and Environmental Sciences, Geophysical Observatory, University of Munchen (2001). *BayernNetz. International Federation of Digital Seismograph Networks*. Other/Seismic Network. <https://doi.org/10.7914/SN/BW10.7914/SN/BW>
- De Verdière, Y. C. (2006). Mathematical models for passive imaging I: General background. *arXiv preprint math-ph/0610043*.
- Derode, A., Larose, E., Tanter, M., de Rosny, J., Tourin, A., Campillo, M., & Fink, M. (2003). Recovering the Green’s function from field-field correlations in an open scattering medium (L). *The Journal of the Acoustical Society of America*, 113(6), 2973–2976. <https://doi.org/10.1121/1.1570436>
- Dziewonski, A., & Anderson, D. (1981). Preliminary reference Earth model. *Physics of the earth and planetary interiors*, 25, 297–356.
- Ebeling, C. W. (2012). 1 Inferring ocean storm characteristics from ambient seismic noise: A historical perspective. *Advances in Geophysics*, 53, 1–33.
- Ekström, G. (2001). Time domain analysis of Earth’s long-period background seismic radiation. *Journal of Geophysical Research*, 106(B11), 26,483–26,493.
- Ermert, L., Villaseñor, A., & Fichtner, A. (2016). Cross-correlation imaging of ambient noise sources. *Geophysical Journal International*, 204(1), 347–364.
- Farra, V., Stutzmann, E., Gualtieri, L., Schimmel, M., & Ardhuin, F. (2016). Ray-theoretical modeling of secondary microseism P waves. *Geophysical Journal International*, 206(3), 1730–1739.



- Friedrich, A., Krüger, F., & Klinge, K. (1998). Ocean-generated microseismic noise located with the Gräfenberg array. *Journal of Seismology*, 2(1), 47–64.
- Fukao, Y., Nishida, K., & Kobayashi, N. (2010). Seafloor topography, ocean infragravity waves, and background Love and Rayleigh waves. *Journal of Geophysical Research*, 115, B04302. <https://doi.org/10.1029/2009JB006678>
- GEOFON Data Centre (1993). *Geofon Seismic Network*. Germany: Deutsches Geoforschungszentrum GFZ. <https://doi.org/10.14470/TR560404>, other/Seismic Network.
- Gerstoft, P., Fehler, M. C., & Sabra K. G. (2006). When Katrina hit California. *Geophysical Research Letters*, 33, L17308. <https://doi.org/10.1029/2006GL027270>
- Gualtieri, L., Stutzmann, E., Farra, V., Capdeville, Y., Schimmel, M., Arduin, F., & Morelli, A. (2014). Modelling the ocean site effect on seismic noise body waves. *Geophysical Journal International*, 197, 1096–1106.
- Hasselmann, K. (1963). A statistical analysis of the generation of microseisms. *Reviews of Geophysics*, 1(2), 177–210.
- Hillers, G., Graham, N., Campillo, M., Kedar, S., Landès, M., & Shapiro, N. M. (2012). Global oceanic microseism sources as seen by seismic arrays and predicted by wave action models. *Geochemistry, Geophysics, Geosystems*, 13, Q01021. <https://doi.org/10.1029/2011GC003875>
- Holcomb, L. G. (1980). Microseisms: A twenty-six-second spectral line in long-period Earth motion. *Bulletin of the Seismological Society of America*, 70(4), 1055–1070.
- Institut de Physique du Globe de Paris (IPGP) (1982). Geoscope, Paris, France: French global network of broad band seismic stations, Institut de Physique du Globe de Paris, (IPGP). <https://doi.org/10.18715/GEOSCOPE.G>, other/Seismic Network.
- Institute of Geophysics, Academy of Sciences of the Czech Republic (1973). Czech regional seismic network, Prague, Czech Republic: International Federation of Digital Seismograph Networks. <https://doi.org/10.7914/SN/CZ>, other/Seismic Network.
- IRIS Transportable Array (2003). USArray Transportable Array. Washington, DC: International Federation of Digital Seismograph Networks. <https://doi.org/10.7914/SN/TA>, other/Seismic Network.
- Juretzek, C., & Hadziioannou, C. (2016). Where do ocean microseisms come from? A study of Love-to-Rayleigh wave ratios. *Journal of Geophysical Research: Solid Earth*, 121, 6741–6756. <https://doi.org/10.1002/2016JB013017>
- Kedar, S., Longuet-Higgins, M., Webb, F., Graham, N., Clayton, R., & Jones, C. (2008). The origin of deep ocean microseisms in the North Atlantic Ocean. *Proceedings of the Royal Society A: Mathematical, Physical and Engineering Sciences*, 464(2091), 777–793. <https://doi.org/10.1098/rspa.2007.0277>
- Kimman, W., & Trampert, J. (2010). Approximations in seismic interferometry and their effects on surface waves. *Geophysical Journal International*, 182(1), 461–476.
- Kimman, W., Campman, X., & Trampert, J. (2012). Characteristics of seismic noise: Fundamental and higher mode energy observed in the northeast of the Netherlands. *Bulletin of the Seismological Society of America*, 102(4), 1388–1399.
- Krischer, L., Megies, T., Barsch, R., Beyreuther, M., Lecocq, T., Caudron, C., & Wassermann, J. (2015). ObsPy: A bridge for seismology into the scientific python ecosystem. *Computational Science & Discovery*, 8(1), 14,003.
- Lin, F.-C., Li, D., Clayton, R. W., & Hollis, D. (2013). High-resolution 3D shallow crustal structure in Long Beach, California: Application of ambient noise tomography on a dense seismic array. *Geophysics*, 78(4), Q45–Q56.
- Longuet-Higgins, B. Y. M. S (1950). A theory of the origin of microseisms. *Philosophical Transactions of the Royal Society of London*, 243(857), 1–35.
- Matsuzawa, T., Obara, K., Maeda, T., Asano, Y., & Saito, T. (2012). Love- and Rayleigh-wave microseisms excited by migrating ocean swells in the North Atlantic detected in Japan and Germany. *Bulletin of the Seismological Society of America*, 102(4), 1864–1871.
- Nishida, K., & Takagi, R. (2016). Teleseismic S wave microseisms. *Science*, 353(6302), 919–921.
- Nishida, K., Kobayashi, N., & Fukao, Y. (2000). Resonant oscillations between the solid Earth and the atmosphere. *Science*, 287(5461), 2244–2246.
- Nishida, K., Kawakatsu, H., Fukao, Y., & Obara, K. (2008). Background Love and Rayleigh waves simultaneously generated at the Pacific Ocean floors. *Geophysical Research Letters*, 35, L16307. <https://doi.org/10.1029/2008GL034753>
- Oliver, J. (1962). A worldwide storm of microseisms with periods of about 27 seconds. *Bulletin of the Seismological Society of America*, 52(3), 507–517.
- RESIF (1981). RESIF-RLBP French Broad-band network, RESIF-RAP strong motion network and other seismic stations in metropolitan France. <https://doi.org/10.15778/RESIF.FR>, other/Seismic Network.
- Rhie, J., & Romanowicz, B. (2006). A study of the relation between ocean storms and the Earth's hum. *Geochemistry, Geophysics, Geosystems*, 7, Q10004. <https://doi.org/10.1029/2006GC001274>
- Roux, P., Sabra, K. G., Gerstoft, P., Kuperman, W., & Fehler, M. C. (2005). P-waves from cross-correlation of seismic noise. *Geophysical Research Letters*, 32, L19303. <https://doi.org/10.1029/2005GL023803>
- Sabra, K. G., Gerstoft, P., Roux, P., Kuperman, W. A., & Fehler, M. C. (2005). Surface wave tomography from microseisms in Southern California. *Geophysical Research Letters*, 32, L14311. <https://doi.org/10.1029/2005GL023155>
- Saito, T. (2010). Love-wave excitation due to the interaction between a propagating ocean wave and the sea-bottom topography. *Geophysical Journal International*, 182(3), 1515–1523.
- Sánchez-Sesma, F. J., & Campillo, M. (2006). Retrieval of the Green's function from cross correlation: The canonical elastic problem. *Bulletin of the Seismological Society of America*, 96(3), 1182–1191.
- Sens-Schönfelder, C., & Wegler, U. (2006). Passive image interferometry and seasonal variations of seismic velocities at Merapi Volcano, Indonesia. *Geophysical Research Letters*, 33, L21302. <https://doi.org/10.1029/2006GL027797>
- Shapiro, N. M., & Campillo, M. (2004). Emergence of broadband Rayleigh waves from correlations of the ambient seismic noise. *Geophysical Research Letters*, 31, L07614. <https://doi.org/10.1029/2004GL019491>
- Shapiro, N. M., Campillo, M., Stehly, L., & Ritzwoller, M. H. (2005). High-resolution surface-wave tomography from ambient seismic noise. *Science*, 307, 1615–1618.
- Shapiro, N. M., Ritzwoller, M., & Bensen, G. (2006). Source location of the 26 sec microseism from cross-correlations of ambient seismic noise. *Geophysical Research Letters*, 33, L18310. <https://doi.org/10.1029/2006GL027010>
- Shen, W., & Ritzwoller, M. H. (2016). Crustal and uppermost mantle structure beneath the United States. *Journal of Geophysical Research: Solid Earth*, 121, 4306–4342. <https://doi.org/10.1002/2016JB012887>
- Slovenian Environment Agency (2001). Seismic network of the Republic of Slovenia, Ljubljana, Slovenia: International Federation of Digital Seismograph Networks. <https://doi.org/10.7914/SN/SL>, other/Seismic Network.
- Snieder, R. (2004). Extracting the Green's function from the correlation of coda waves: A derivation based on stationary phase. *Physical Review E*, 69(4), 46,610.
- Sorensen, R. M. (2005). *Basic Coastal Engineering*. Springer.

- Stehly, L., Campillo, M., & Shapiro, N. (2006). A study of the seismic noise from its long-range correlation properties. *Journal of Geophysical Research*, 111, B10306. <https://doi.org/10.1029/2005JB004237>
- Stutzmann, E., Roullet, G., & Astiz, L. (2000). Geoscope station noise levels. *Bulletin of the Seismological Society of America*, 90(3), 690–701.
- Swiss Seismological Service (SED) at ETH Zurich (1983). National seismic networks of Switzerland, Swiss Seismological Service, Switzerland. [https://doi.org/10.12686/sed/networks/ch\\_other/Seismic\\_Network](https://doi.org/10.12686/sed/networks/ch_other/Seismic_Network)
- Tian, Y., & Ritzwoller, M. H. (2015). Directionality of ambient noise on the Juan de Fuca Plate: Implications for source locations of the primary and secondary microseisms. *Geophysical Journal International*, 201(1), 429–443.
- Wapenaar, K. (2004). Retrieving the elastodynamic Green's function of an arbitrary inhomogeneous medium by cross correlation. *Physical Review Letters*, 93(25), 254,301.
- Wapenaar, K., Slob, E., & Snieder, R. (2006). Unified Green's function retrieval by cross correlation. *Physical Review Letters*, 97(23), 234301.
- Weaver, R. L., & Lobkis, O. I. (2001). On the emergence of the Green's function in the correlations of a diffuse field. *The Journal of the Acoustical Society of America*, 109(5), 2410–2410.
- Weaver, R. L., & Lobkis, O. I. (2004). Diffuse fields in open systems and the emergence of the Green's function (I). *The Journal of the Acoustical Society of America*, 116(5), 2731–2734.
- Webb, S. C. (1998). Broadband seismology and noise under the ocean. *Reviews of Geophysics*, 36(1), 105–142.
- Yang, Y., & Ritzwoller, M. H. (2008). Characteristics of ambient seismic noise as a source for surface wave tomography. *Geochemistry, Geophysics, Geosystems*, 9, Q02008. <https://doi.org/10.1029/2007GC001814>
- Zeng, X., & Ni, S. (2010). A persistent localized microseismic source near the Kyushu Island, Japan. *Geophysical Research Letters*, 37, L24307. <https://doi.org/10.1029/2010GL045774>
- Zeng, X., & Ni, S. (2011). Correction to "A persistent localized microseismic source near the Kyushu Island, Japan". *Geophysical Research Letters*, 38, L16320. <https://doi.org/10.1029/2011GL048822>
- Zeng, X., & Ni, S. (2014). Evidence for an independent 26-s microseismic source near the Vanuatu Islands. *Pure and Applied Geophysics*, 171(9), 2155–2163.
- Zheng, Y., Shen, W., Zhou, L., Yang, Y., Xie, Z., & Ritzwoller, M. H. (2011). Crust and uppermost mantle beneath the north China craton, northeastern China, and the sea of Japan from ambient noise tomography. *Journal of Geophysical Research*, 116, B12312. <https://doi.org/10.1029/2011JB008637>